九州大学学術情報リポジトリ
Kyushu University Institutional Repository

# Full noninductive plasma start-up using electron Bernstein wave current drive on high-field side injection in QUEST

Zhou, Junyao
Interdisciplinary Graduate School of Engineering Sciences, Kyushu University

Hanada, Kazuaki
Research Institute for Applied Mechanics, Kyushu University

Onchi, Takumi
Research Institute for Applied Mechanics, Kyushu University

Kojima, Shinichiro
National Institutes for Quantum Science and Technology

他

https://hdl.handle.net/2324/7437065

出版情報：Nuclear Fusion. 66 (8), 2026-07-13. IOP Publishing
バージョン：
権利関係：Creative Commons Attribution 4.0 International

KYUSHU UNIVERSITY

nuclear fusion
IAEA

PAPER • OPEN ACCESS

# Full noninductive plasma start-up using electron Bernstein wave current drive on high-field side injection in QUEST

To cite this article: Zhou Junyao *et al* 2026 *Nucl. Fusion* **66** 086019

View the article online for updates and enhancements.

You may also like

- Flux pumping and bifurcated relaxations of helical core in 3D magnetohydrodynamic modelling of ASDEX Upgrade plasmas
H. Zhang, M. Hoelzl, I. Krebs et al.
- TGLF-WINN: data-efficient deep learning surrogate for turbulent transport modeling in fusion
Yadi Cao, Futian Zhang, Wesley Liu et al.
- Recent advances in plasma control and physics research in the Large Helical Device
K. Tanaka, K. Ida, Y. Morishita et al.

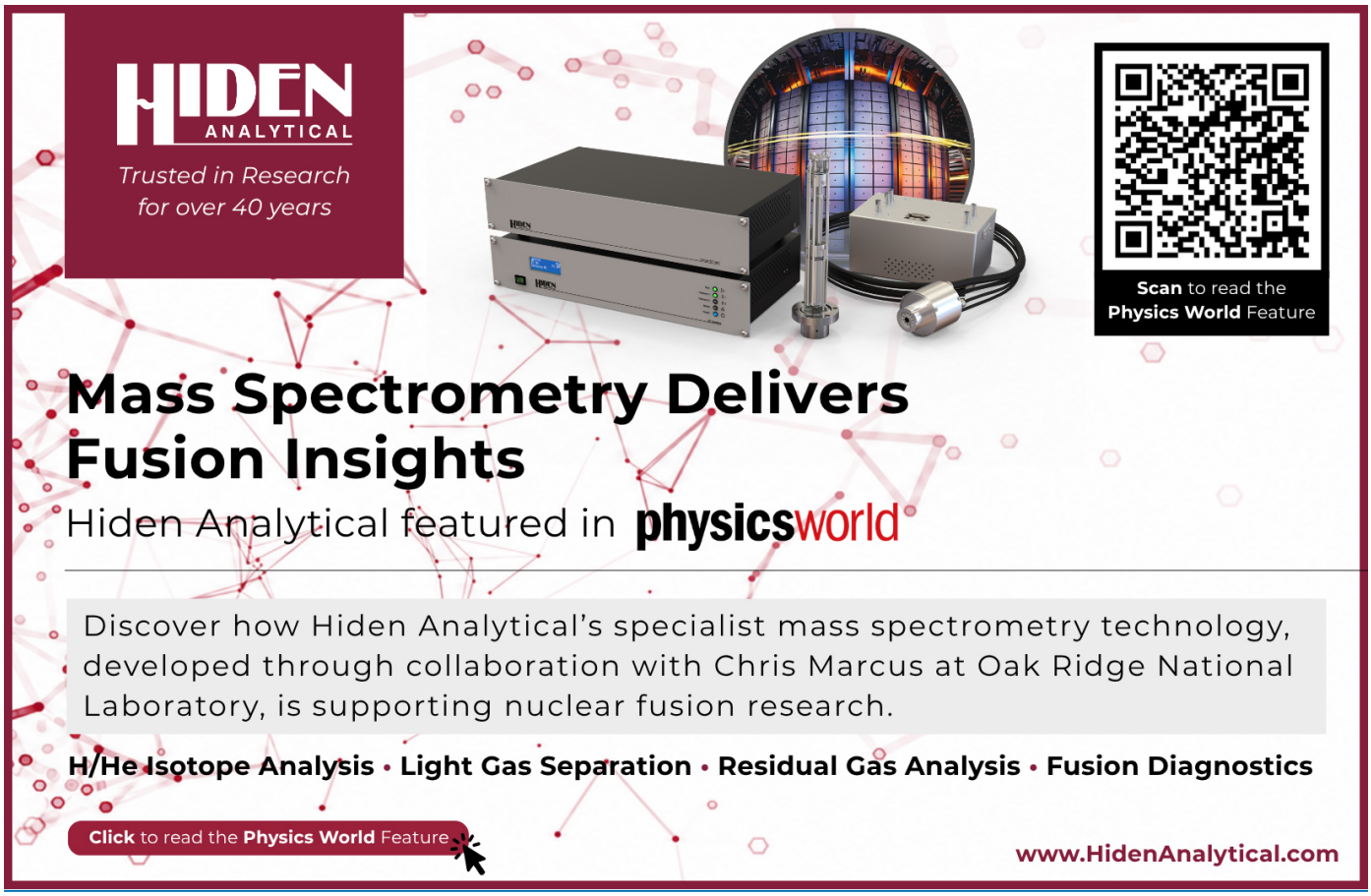


This content was downloaded from IP address 133.5.178.225 on 27/07/2026 at 01:52

OPEN ACCESS
IOP Publishing | International Atomic Energy Agency
Nuclear Fusion
Nucl. Fusion **66** (2026) 086019 (16pp)
https://doi.org/10.1088/1741-4326/ae7b57

# Full noninductive plasma start-up using electron Bernstein wave current drive on high-field side injection in QUEST

**Zhou Junyao[1,*], Hanada Kazuaki[2], Onchi Takumi[2], Kojima Shinichiro[3], Yue Qilin[1], Kuroda Kengoh[4], Kono Kaori[2], Ido Takeshi[2], Ikezoe Ryuya[2], Hasegawa Makoto[2], Idei Hiroshib[2], Nagashima Yoshihiko[2], Sekiya Izumi[2], Kinoshita Toshiki[2], Higashijima Aki[2], Nagata Takahiro[2] and Seiya Sakai[2]**

[1] Interdisciplinary Graduate School of Engineering Sciences, Kyushu University, Fukuoka, Japan
[2] Research Institute for Applied Mechanics, Kyushu University, Fukuoka, Japan
[3] National Institutes for Quantum Science and Technology, Chiba, Japan
[4] Japan Coast Guard Academy, Kure, Japan

E-mail: j.zhou@triam.kyushu-u.ac.jp

Received 12 January 2026, revised 24 May 2026
Accepted for publication 10 June 2026
Published 13 July 2026

**Abstract**

Electron cyclotron wave (ECW) injection is considered an effective auxiliary method for plasma start-up. In QUEST, high-field side (HFS) injection of ECW was conducted to achieve effective mode conversion to electron Bernstein wave (EBW), which can propagate in high-density plasma and provide greater heating/current-drive efficiency than ECW at low electron temperatures. The EBW-driven current, $I_{EBW}$, whose direction is inverted by toroidal and radial magnetic fields, was clearly observed experimentally, and this characteristic of EBW current drive (EBWCD) played an important role in closed-flux surface formation. The findings are supported by an improved current-density profile model used to reconstruct the current distribution in the open flux surface (OFS) phase. The EBWCD efficiency in the OFS is approximately evaluated 0.014 A $W^{-1}$ in the OFS phase using a model calculation that includes co- and counter-directed $I_{EBW}$.

Keywords: spherical tokamak (ST), noninductive plasma start-up, electron Bernstein wave (EBW), electron Bernstein wave current drive (EBWCD), high-field side (HFS), QUEST

(Some figures may appear in colour only in the online journal)

* Author to whom any correspondence should be addressed.

Original content from this work may be used under the terms of the Creative Commons Attribution 4.0 licence. Any further distribution of this work must maintain attribution to the author(s) and the title of the work, journal citation and DOI.

## 1. Introduction

Spherical tokamaks (STs) are characterized by a higher $\beta$-limit than conventional tokamaks, making them a cost-effective candidate for fusion power plants [1]. While, ST based fusion power plants require effective noninductive plasma start-up due to the limited space for central solenoids. Noninductive current drive by RF injection is considered a promising method.

Electron cyclotron wave (ECW) [2, 3] is useful for plasma initiation in tokamaks, but their effectiveness is low in present ST plasmas, which have lower magnetic fields and higher dielectric constants than conventional tokamaks. The narrow space in the central part of the torus results in a low toroidal field, requiring the use of low-frequency ECW, which is more likely to encounter cutoffs induced by plasma properties. This makes it difficult to obtain high-density plasmas. On the other hand, the electron Bernstein wave (EBW) do not have cutoff issues and can be generated from ECW through mode-conversion processes. Moreover, because it propagates as an electrostatic wave, EBW can heat plasma and drive the plasma current, $I_{\mathrm{p}}$ more efficiently at low temperatures. This is essential for forming closed flux surface (CFS) [4–7].

Several mode-conversion scenarios have been proposed, including ordinary–eXtraordinary–Bernstein (O–X–B) mode conversion from low-field side (LFS) [8–10] and X–B mode conversion from the LFS [11]. The O-mode ECW is converted to X-mode at the plasma cutoff, and the X-mode is further converted to EBW at the upper hybrid resonance (UHR) layer. However, because this process requires two conversions, it is difficult to achieve a high mode-conversion efficiency without precise ECW injection angle adjustment. During the plasma startup phase, the plasma density fluctuates significantly, making the adjustment process more complex. X–B mode conversion from the LFS requires a steep density gradient [12], which is not expected just after the plasma initiation. X–B mode conversion from the high-field side (HFS) [13–15] offers significant advantages for achieving a high mode-conversion efficiency without requiring an extremely steep density gradient or complicated ECW injection angle adjustments. Nevertheless, installing an injection system on the HFS is challenging due to the limited space for antennas compared to LFS.

So far, EBW applications in tokamaks have been studied on several devices [16–20]. The first demonstration was conducted in the COMPASS-D tokamak device using a 60 GHz ECW system, where the launch angle of the injected X-mode wave was set as a variable. The results show that EBWH/EBW current drive (EBWCD) achieved the highest efficiency when the wave was injected perpendicularly [16]. In the MAST device, the presence of EBWCD was demonstrated, showing that the CD direction could be modified by the radial magnetic field ($B_{\mathrm{R}}$), which is a typical feature of EBWCD as described below [17–19]. In the LATE device, noninductive start-up with EBW shows that by placing the first and second ECR layers near the plasma core and the outer vessel wall, respectively, the plasma can be heated efficiently and the line-averaged electron density, exceeds approximately six times the plasma cutoff density [20].

In QUEST, an over-dense plasma exceeding the cutoff density ($n_{\mathrm{e}}$ (O-cutoff) $= 0.83 \times 10^{18}$ m$^{-3}$ for 8.2 GHz) with an $I_{\mathrm{p}}$ above 4 kA was successfully achieved using 8.2 GHz EBW-assisted plasma start-up by HFS injection [14, 15]. Studies on EBWCD has primarily focused on the CFS phase, because EBWCD plays a significant role in sustaining the plasma. While, it is also applicable to plasma start-up phase, and its mechanism in the open flux surface (OFS) phase remains unclear.

The EBW drives the plasma current according to the refractive index parallel to the magnetic field, $N//$. The value of $N//$ is given by $N_{\parallel} = N_{\Phi} R + (N_{\mathrm{R}} B_{\mathrm{R}}/B)$ near the ECR layer [21], where, $N_{\Phi}$, $N_{\mathrm{R}}$ indicate the refractive indices to the toroidal and radial direction, respectively, and $B$ denotes the magnetic field strength. In the EBW power absorption region, the second term becomes to be dominant. As a result, the EBWCD is likely to be composed of forward and reversed currents according to $B_{\mathrm{R}}$. When the direction of EBWCD coincides with the direction of pressure-driven current, $I_{\mathrm{pressure}}$, CFS formation may be promoted. Here the $I_{\mathrm{pressure}}$ is mainly consist of the Pfirisch-Schlüter current in the OFS configuration, which flows along the magnetic field lines and is driven by the plasma pressure gradient. While, EBWCD drives current in the opposite direction to $I_{\mathrm{pressure}}$, it may hinder CFS formation through the reduction of total current, but the EBWCD helps concentrate $I_{\mathrm{p}}$ distribution by canceling the widespread $I_{\mathrm{pressure}}$. The focused $I_{\mathrm{p}}$ Willplay a key role in CFS formation. As described above, the properties of EBWCD in the OFS configuration should be investigated. If the properties predictively work, Br control may be essential for effective plasma start-up, forming a CFS. Identifying the optimal magnetic field configuration for EBWCD-assisted plasma start-up is useful for future tokamak-based fusion devices.

In this study, $B_{\mathrm{T}}$ inversion was also used to distinguish EBW driven current, $I_{\mathrm{EBW}}$, from $I_{\mathrm{pressure}}$. The magnetic flux distribution in the OFS phase was measured with flux loops on the vacuum vessel surface and reconstructed with the improved current profile model [22]. The $B_{\mathrm{R}}$ was applied to correct the error field caused by TF coil junctions and to optimize EBWCD start-up by adjusting the current-drive area. As a result, the conditions for the smooth ramp-up of $I_{\mathrm{p}}$ were clarified.

In this paper, the experimental apparatus and situation is introduced in the section 2, and the experimental results is described in the section 3. The current density reconstruction and relating discussion are shown in the section 4 and 5, and the summary of the contents is given in the section 6.

## 2. EBWCD experiment on HFS injection

This EBWCD experiment with HFS injection was conducted on the ST device QUEST with $R = 0.64$m and $a = 0.36$m. Eight symmetrical 2-turn TF coils were installed outside the

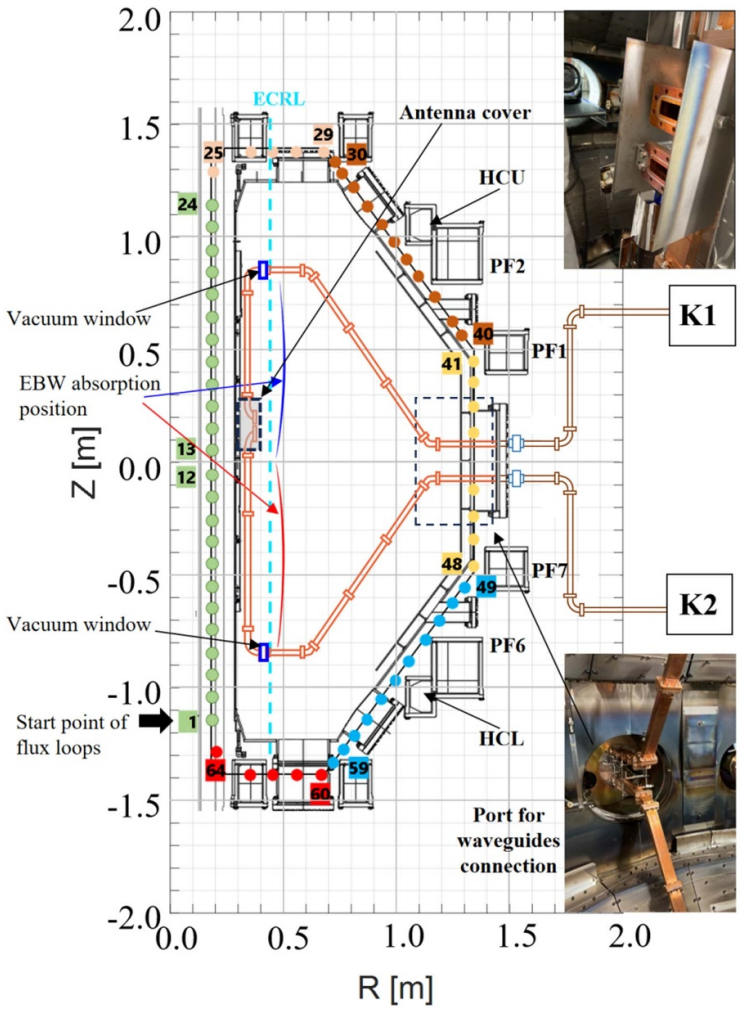


**Figure 1.** Atmospheric waveguides (brown) and vacuum waveguides (orange) in QUEST. $SF_6$ gas was filled inside the vacuum waveguides to prevent arcing. The Saphir vacuum windows were set at the HFS of the ECR layer to isolate the $SF_6$ gas. K1 and K2 are klystrons, providing 25 kW/8.2 GHz power output, respectively. Colored points indicate magnetic flux loops distributed on the vacuum vessel wall. The black arrow marks the starting point of the flux loop distribution, with subsequent numbering following a CW sequence. Green points (C1–24) located on the center stack are the most sensitive flux loops to EBW drive current. Among them, loops 12 and 13 are located on the lower and upper sides of the equatorial plane, respectively. The pink (T25–29) and red (B60–64) points are the symmetrical loops located on the top and bottom sides inside the vacuum vessel. The brown (TS 30–40) and blue (BS49–59) points lie on the inclined surface inside the vacuum vessel. The yellow points (S41–48) are located on the farthest surface of the vacuum vessel. The predicted EBW power absorption regions are also shown: blue represents EBWCD generated in CW, red indicates EBWCD generated in CCW for $B_R = \pm 5$ mT in the case of $B_T$ [CCW].

vacuum vessel, five pairs of PF coils were symmetrically distributed along its equatorial plane (PF1 and PF7 with 12 turns each, PF2 and PF6 with 36 turns each were used in this study), and one pair of 16-turn HCU and HCL coils generated $B_R$ (figure 1). The current of the PF coil pair remains equal in both magnitude and direction, but the current of the HCU and HCL coil pair, while equal in magnitude, is in opposite directions, generating a BR. The sign of $B_R$ in this paper is defined as positive (inward) and negative (outward). In this paper, the inward $B_R$ is shown in cool colors, and the outward $B_R$ in warm colors to identify visually (figure 2). The directions of coil current and $I_p$ (clockwise, CW; counter-clockwise, CCW) are defined from the top-view and CW current is expressed as a negative value. The toroidal magnetic field in the CCW direction from the top-view is denoted as $B_T$ [CCW].

PF coils 1–7 ($-30$ A $\times$ 12 turns) and 2–6 (167 A $\times$ 36 turns) were used to generate a vertical magnetic field of $B_v = 2$ mT and $n-$ index $= 0.35$ at $R = 0.6$m on the mid-plane. TF coil currents of 42 kA per turn were used to produce $B_T = 0.22$T at $R = 0.64$ m, and the first ECR layer for 8.2 GHz ECW was located at $R = 0.45$m. The settings were chosen to optimize the best performance of plasma start-up without $B_R$ in the previous studies on QUEST [15]. A dedicated HFS injection system was installed in the vacuum vessel to inject X-mode ECW into the plasma from the HFS (figure 1). Al and Cu waveguides were used on the atmospheric side, while Cu vacuum waveguides were installed on the vacuum side (figure 1). A Saphir vacuum window was placed in the HFS of the first ECR layer. The waveguides were filled with $SF_6$ gas to prevent arcing, and the vacuum window was used to prevent $SF_6$ leakage into

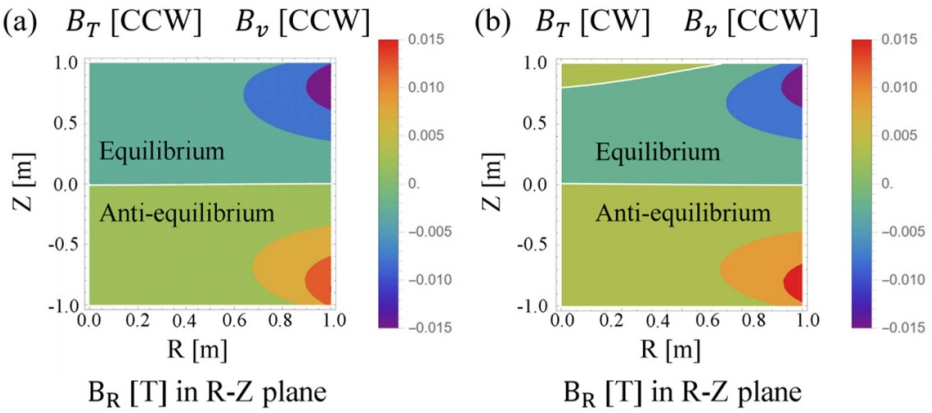


**Figure 2.** $B_R$ profile in the vacuum magnetic configuration. PF coils were energized with −30 A in PF1–7 (12 turns) and 167 A in PF2–6 (36 turns). The cold and warm zones represent the area where $B_R$ is directed inward and outward relative to the center of the vacuum vessel, respectively. The white line denotes the location where $B_R = 0$. The equilibrium and anti-equilibrium areas indicate where the EBW is expected to drive the current in the same or opposite direction as the equilibrium current. The $I_{pressure}$ always flows in the equilibrium direction.

the vacuum vessel. Tungsten covers were equipped on both sides of the antenna to protect it from plasma (see the inset of figure 1). The antenna is located 0.17 m above the mid-plane, and the cover protecting the antenna protrudes further towards the plasma. Since it is significantly close to the plasma, its influence on the plasma may be far from insignificant. The current distribution model assumes that no current passing through the antenna cover, and takes some of its effects into consideration. This paper describes a dedicated experiment to identify the effects of EBWCD during the start-up phase. In future fusion devices, if the method described in the paper is to be used, it is extremely important to improve the method of injecting ECW so as not to affect the plasma as proposed in the previous papers [16, 19].

Two klystrons, each with 25 kW/8.2 GHz power output, were employed. The antennas, positioned 0.17 m above the mid-plane of the vacuum vessel, were protected from plasma by the covers made of tungsten. The rear edge of the cover is flush with the center stack, while the front edge is positioned at $R = 0.363$ m, and the upper and lower edges at $Z = 0.28$ m and $Z = 0.06$ m, respectively. According to calculations by [13], the ECW incident here is expected to be converted into EBW and propagate primarily to the upper side of the plasma, efficiently driving $I_p$. Mineral-Insulated cables with high heat and vacuum resistance were used as conductor wires for magnetic diagnostics, wound into a toroidal loop on the vacuum vessel wall. The vertical magnetic fluxes, primarily generated by $I_p$ and PF coil currents, were measured by 64 flux loops (figure 1).

Changes in $I_p$ or PF coil currents alter the vertical magnetic flux, generating a voltage signal of flux loops. Integrating a flux loop signal provides the time evolution of magnetic flux at the position, which was used for current profile fitting [22].

Flux loops were installed on the center stack every 0.1 m from $Z = 1.15$m to $-1.15$ m, totaling 24 (C1–24, figure 1). These 24 coils, positioned near the predicted ECR layer ($R = 0.45$m) and EBW absorption regions, are also sensitive to $I_{EBW}$. Their signals were recorded with an oscilloscope (DL850 type Yokogawa Electric Corp.) at a proper sampling frequency of 100 kS $s^{-1}$ for accurate integration. Despite efforts, the integrated signals often contained a drift component caused by high-frequency noise exceeding the sampling frequency. To remove the drift component, a time-linear fit before and after each discharge was applied, and the drift was mostly subtracted from the magnetic flux signals. In addition, off-plasma discharges that under the same magnetic fields but without plasma were also conducted to obtain plasma-induced magnetic flux signals for each discharge. The PF coil contribution was completely subtracted from the magnetic flux and the plasma-induced magnetic flux was successfully obtained.

Figure 2 shows the $B_R$ profile of the vacuum magnetic configuration under the typical experimental conditions. The $N_{||}$ of the EBW near the first ECR layer is expressed as:

$$N_{||} = N_\Phi R + N_R B_R / B,$$

and its direction is primarily influenced by $B_R$, as $N_R$ increases significantly around the first ECR layer. The direction of the $I_{EBW}$ reverses when the $B_T$ is reversed, since the sign of $N_{||}$ primarily depends on the direction of $B_T$. Figure 2(*a*)) shows the $B_R$ profile for the $B_T$ [CCW] configuration, with the equilibrium $I_{EBW}$ expected to flow along the upper side of the plasma. In contrast, under the $B_T$ [CW] configuration (figure 2(*b*)), the equilibrium $I_{EBW}$ flows in the lower side of plasma. The equilibrium $I_p$ direction changed with $B_v$ but the region of the equilibrium current remains unchanged, where $B_v$ denotes a vertical magnetic field. Because the $B_R$ direction reverses, when the $B_v$ is reversed.

As the direction of the $I_{pressure}$ also changes in the $B_V$, distinguishing the $I_{EBW}$ from the $I_{pressure}$ using $B_v$ reversal is impossible. For example, comparing the case 1 and case 4 in figure 3, the EBWCD in the equilibrium direction is expected to flow on the upper side, while $I_{pressure}$ flows in the equilibrium direction on both sides. When the $B_V$ direction is reverse, the EBWCD direction is also reversed, but the equilibrium direction also reverses. Consequently, the EBWCD in

| | $B_T$ | $B_V$ | $I_P$ | Top | Bottom |
|---|---|---|---|---|---|
| Case 1 | CCW | CCW | CW | Eq | Anti |
| Case 2 | CW | CCW | CW | Anti | Eq |
| Case 3 | CW | CW | CCW | Anti | Eq |
| Case 4 | CCW | CW | CCW | Eq | Anti |

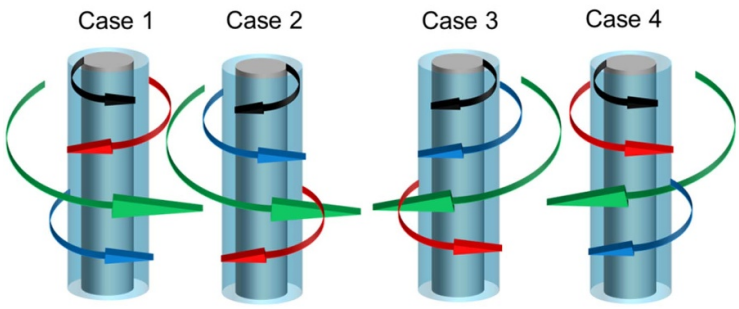


**Figure 3.** (a) Black arrows represent the direction of $B_T$, green arrows represent the direction of $B_v$, red arrows represent the direction of equilibrium $I_{EBW}$ and blue arrows represent the direction of anti-equilibrium $I_{EBW}$. (b) The magnetic configuration to investigate plasma start-up using EBWCD.

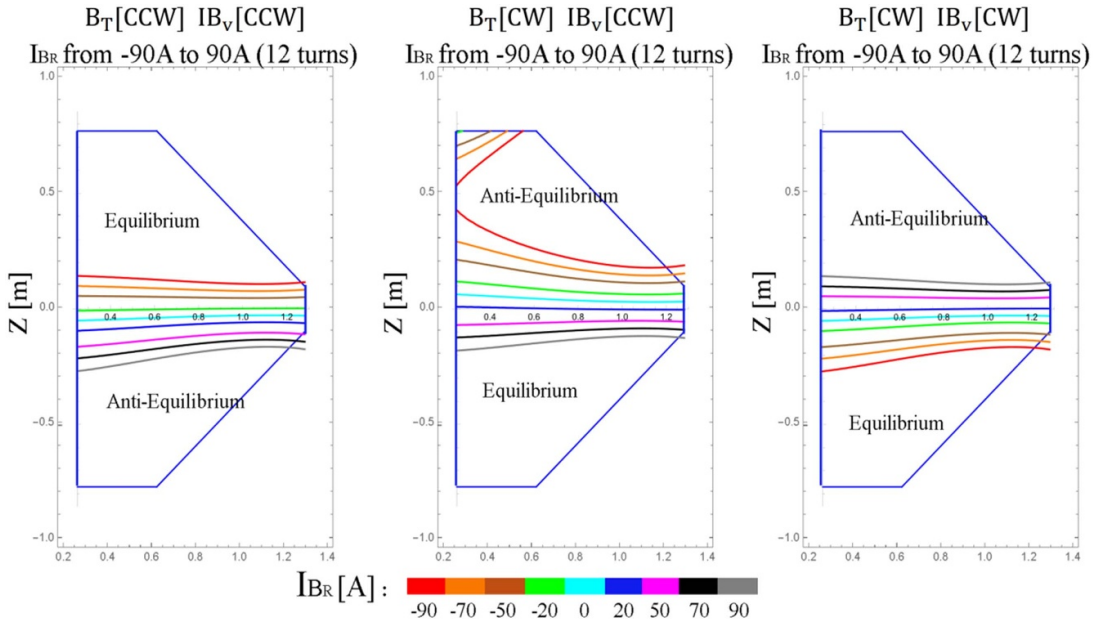


**Figure 4.** Equilibrium and anti-equilibrium areas for EBWCD under various magnetic field configurations generated by different coil currents in the paired HCU and HCL coils, $I_{BR}$. The lines indicate the $B_R = 0$ boundaries corresponding to each HCU and HCL coil current. The line colors denote the applied current values, as indicated by the color bar at the lower side. The blue frame represents the plasma boundary determined using the dedicated waveguides and the vacuum vessel used in this study (figure 1).

the equilibrium direction remains on the upper side. This is why the $B_T$ inversion is needed to distinguish the $I_{EBW}$ from the $I_{pressure}$. As a result, there are four types of magnetic field configurations that need to be investigated as shown in figures 3(a) and (b). Reversing the $B_T$ is essential as shown in case 1 and case 2. In the paper, the cases 1–3 were mainly performed. Minor differences between both magnetic configurations (figure 4) are primarily attributed to the $B_R$ generated by the incomplete compensation of the one-turn toroidal component of the TF coil. By adjusting the HCU and HCL coil currents within the range of $\pm 90$ A, the ratio of the equilibrium to anti-equilibrium area of the $I_{EBW}$ can be controlled.

For quantitative analysis, the ratio of the equilibrium area to the anti-equilibrium was calculated. While this index provided only an approximate evaluation, since each area should uniformly be weighted only by the EBW power deposited regions, it remains valuable for illustrating a schematic figure of merit within the complex magnetic configuration (figure 4).

The $B_R$ was varied by adjusting the HUC and HCL coil currents from $-90$ A to 90 A, resulting in changes in the equilibrium and anti-equilibrium areas of the EBWCD (figure 4). The $I_p$ was confined within the region denoted by the blue lines, since the waveguides also served as limiters inside the vacuum vessel. Electrons striking the waveguides prevented

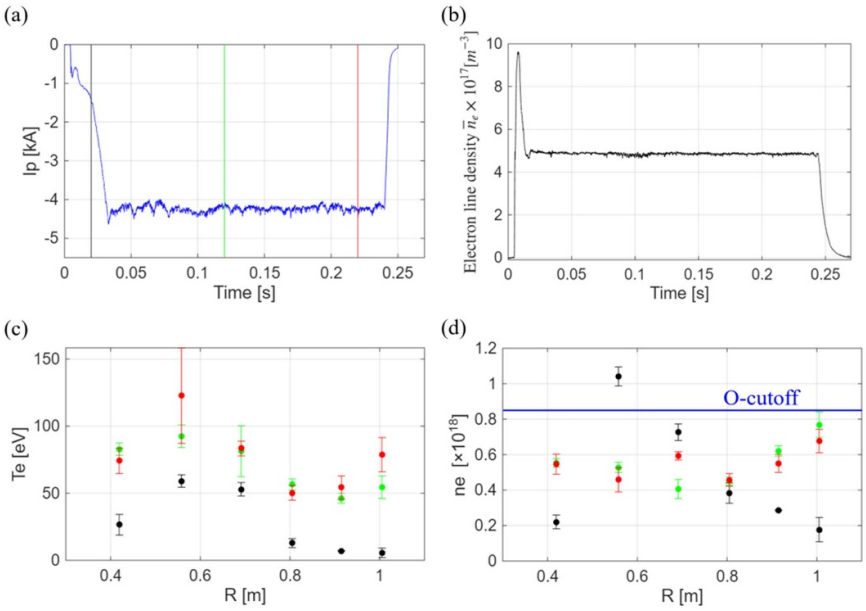


**Figure 5.** (*a*) Time evolution of $I_p$ under $B_T$ [CW] and $B_v$ [CCW] (case 2). The steady currents of PF26, PF17, and $I_{BR}$ were applied and the values were 116.7 A (36 turns), −29.9 A (12 turns), and −20 A (16 turns), respectively. Black, green and red lines denote the time points of 0.02 s, 0.12 s and 0.22 s after RF injection. (*b*) $\bar{n}_e$ measured by interferometer. (*c*) $T_e$ measured by Thomson scattering at the time points, whose color is corresponding to the line color in (*a*). (*d*) $n_e$ measured by Thomson scattering at the time points, whose color is corresponding to the lines in (*a*). The plasma cutoff ($(\omega_{pe}/\omega)^2 \cong 1$) are indicated in panel.

the formation of a net current. In the future, we will optimize the installation method of the waveguides so that they do not affect the plasma configuration inside the vacuum vessel. To apply this technique to fusion experiments, it would be necessary to launch the ECW from top or bottom high field side [16] or install mode-conversion mirrors on the central stack [19].

## 3. Experiment results

Figure 5 shows time evolutions of $I_p$ in a typical discharge under $B_T$ [CW] and $B_v$ [CCW]. $T_e$ and $n_e$ at 0.02 s, 0.12 s and 0.22 s after RF injection was measured by Thomson scattering. Two peaks of $T_e$ and ne were observed at 0.12 s and 0.22 s. This indicates a CFS was formed and these peaks were located on the same magnetic surface.

Figure 6(*a*)) shows the time evolutions of the $I_p$ in the cases of $B_T$ [CCW] (case 1) and $B_T$ [CW] (case 2). For the $B_T$ [CCW] configuration (case 1), $I_p$ remained constant or exhibited a slight negative growth during the OFS phase (0–0.05 s) following the initial fluctuation indicated by the red arrow. Subsequently, it increased significantly to its maximum value after the oscillation marked by the red circle, suggesting the formation of a CFS [23]. For the $B_T$ [CW] (case 2), $I_p$ exhibited sustained growth without oscillations until the CFS formed, contrasting significantly with the current jump observed under the $B_T$ [CCW] (case 1) [23]. Figure 6(*b*)) shows the $I_p$ growth rate denoted by the black dashed frame (figure 6(*a*)). The $I_p$ growth rate was calculated by applying a moving average to the measured current data. The sampling of the current was executed every $2 \times 10^{-6}$ s. The moving average uses 1500 samples. The error bar was determined by the maximum and minimum $I_p$ growth rates within the black dashed frame For the $B_T$ [CCW], $I_p$ remained nearly constant or even decreased before abruptly increasing to its maximum value. On the other hand, for $B_T$ [CW], $I_p$ increased continuously, with a growth rate >17 kA $s^{-1}$. As a distinct boundary was observed, the $I_p$ behaviors during the OFS phase for $B_T$ [CCW] (case 1) and $B_T$ [CW] (case 2) are designated 'jump' and 'ramp-up,' respectively, in this study.

Figure 7(*a*) shows the magnetic flux distribution induced by only plasma current at 0.02 s after the initiation of an RF injection. The corresponding time point (figure 6, black arrow) was evaluated to minimize the effect of eddy currents on the plasma-facing components and the vacuum vessel, including the central stack, which is made of SS type 316 l and lacks toroidal insulation. The horizontal axis represents the number of the flux loop, corresponding to the spatial distribution in figure 1. Figure 7(*b*)) illustrates an expanded plot of the magnified flux signals measured only on the central stack. For the $B_T$ [CCW] (case 1), the flux signals peaked in the equilibrium direction on the upper side. In contrast, the peak for the equilibrium direction was on the lower side in $B_T$ [CW] (case2). A slight peak shift was observed on the LFS near ch44, where the EBW antenna was positioned. This tendency that peaks on HFS and LFS moved with the inversing of $B_T$ is theoretically expected (figure 2), which demonstrate the changing location of current concentration.

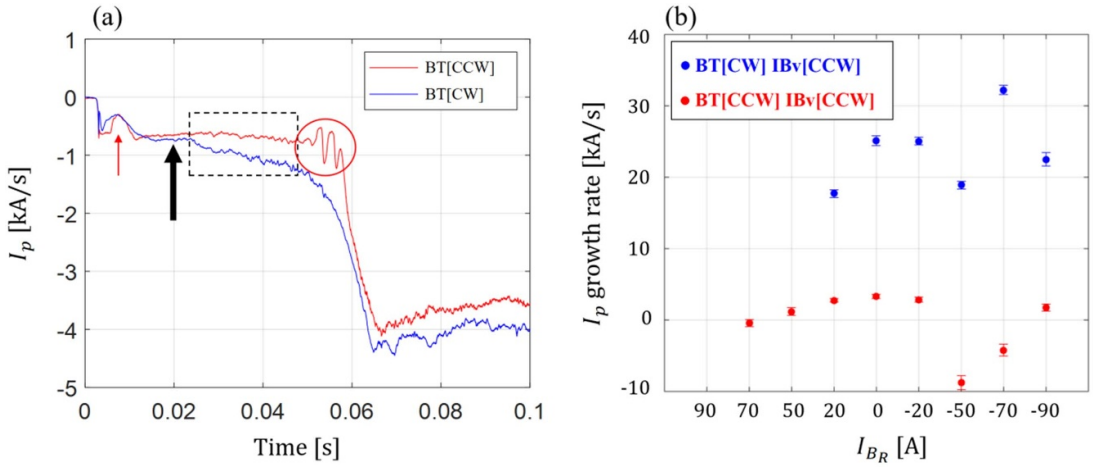


**Figure 6.** (*a*) Time evolution of $I_p$ for different $B_T$ directions at PF17 current = −29.9 A (12 turns), PF26 current = 116.7 A (36 turns), and $I_{BR} = 0$ A (case 1 and 2). The $B_R$ profiles are denoted in figure 2. The red and blue lines represent $I_p$ measured with a Rogowski coil in $B_T$ [CCW], $I_{BV}$ [CCW] (case 1), $I_{BR} = 0$ A and $B_T$ [CW], $I_{BV}$ [CCW] (case 2), $I_{BR} = 0$ A, respectively. The black arrow indicates the time point with the flux data plotted in figure 7(*b*) $I_p$ growth rates from 0.025 s to 0.05 s which is indicated by the black dashed frame for $B_T$ [CCW] and $B_T$ [CW] configurations (case 1 and 2), with $I_{BR}$ varying from −90 A to 90 A.

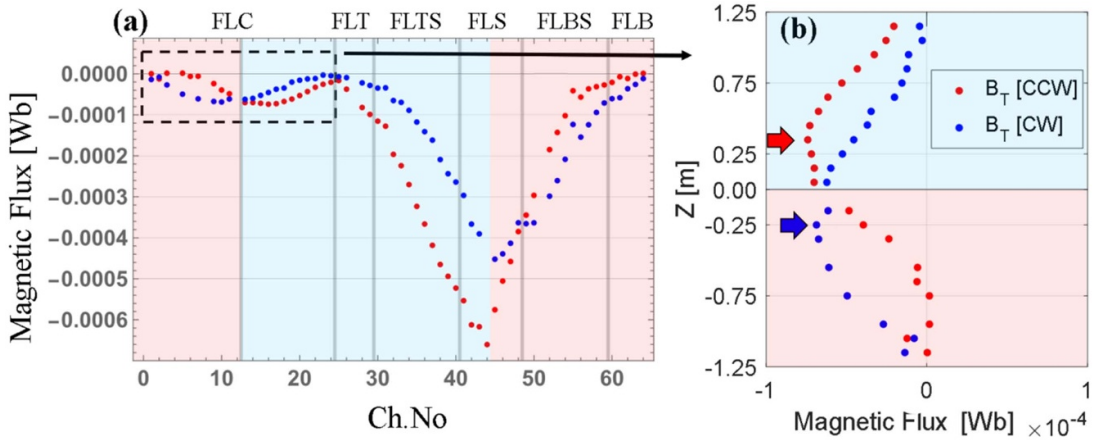


**Figure 7.** Magnetic flux distribution at the time indicated by the arrow in figure 6. (*a*) Flux distribution for all 64 channels. FLC, central stack flux loop; FLT top flux loop; FLTS, top-side flux loop; FLBS, bottom-side flux loop; FLB, bottom flux loop. (*b*) Enlarged view of the 24ch signal on the central stack surface plotted along the *Z* direction. The small red and blue arrow in (*b*) indicate the peak locations of the flux distribution in the equilibrium direction. The light blue and light red shaded areas in (*a*) and (*b*) represent the flux loops located above or below the mid-plane, respectively.

Figure 8 illustrates the time evolution of $I_p$ corresponding to various $B_R$. An index, termed the area ratio, was introduced to quantitatively represent the figure of merit of the configuration and is defined as:

$$\text{Area ratio} = \frac{\text{Equilibrium area} - \text{AntiEquilibrium area}}{\text{Equilibrium area} + \text{AntiEquilibrium area}}.$$

For all magnetic configurations, $I_p$ consistently initiated once the area ratio became positive, indicating that the equilibrium area was greater than the anti-equilibrium area. Figures 8(*b*) and (*c*) show that $I_p$ in the OFS phase transitioned from a constant value to a ramp-up phase (figure 6) and reached its maximum earlier with increasing area ratio. The error bar (figure 8(*c*)) at 0.03 s was larger than in other cases, potentially attributed to the rapid growth of $I_p$. These findings indicate that a larger equilibrium area facilitates plasma start-up. An exception was observed at an area ratio of 0.365 (figure 8(*a*)), where $I_p$ failed to initiate. This operation was not repeated multiple times during the experiment; therefore, its reproducibility could not be confirmed. It should be noted that in this experiment, the plasma was reproducible well, and even after restoring the parameters after scanning, almost the same plasma was reproduced. Since the failed discharge was the last one performed in the day's experiment, and all previous discharges had successfully started the plasma. It suggested that the wall conditioning was not the cause of the failure. Since the plasma failed to start, it was difficult to compare the line spectrum emitted from the impurities with that emitted from a successfully started discharge. The cause of the failure may be that the plasma potentially deviated upward during the early phase due to the large $B_R$, disrupting the current upon contact with the waveguides inside the vacuum vessel.

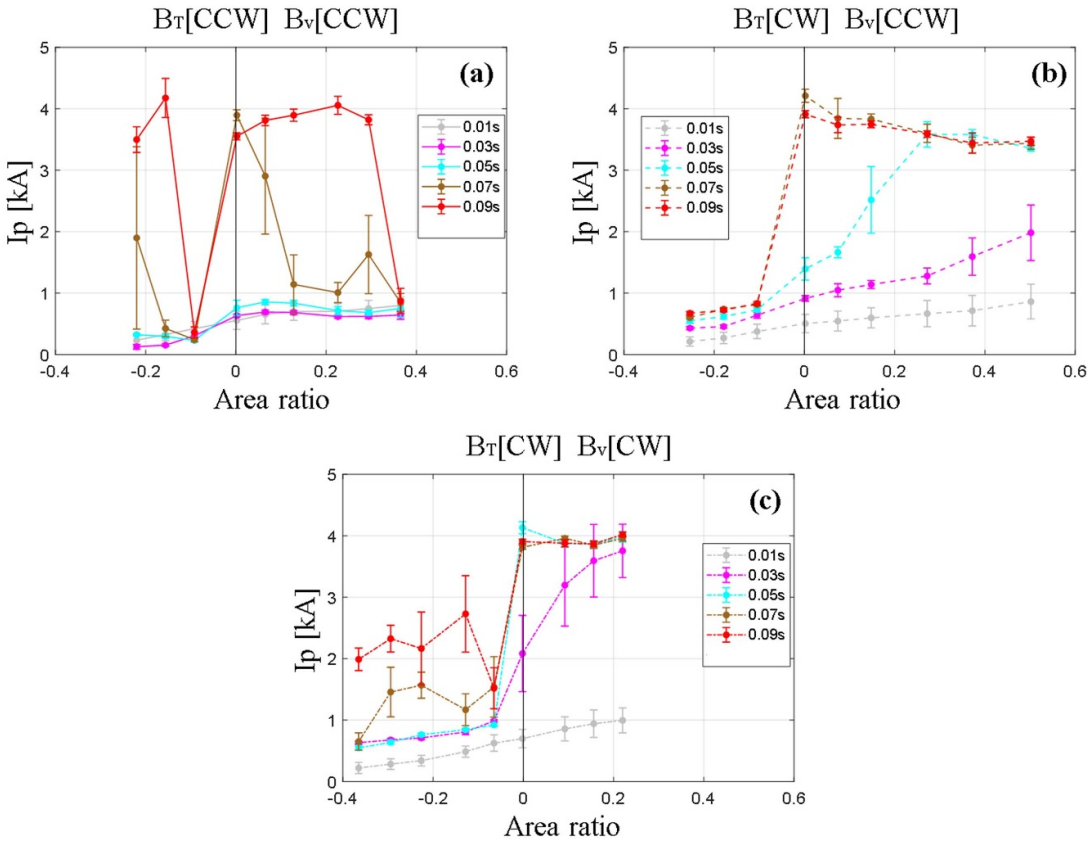


**Figure 8.** $I_p$ at different time points for various $B_R$ configurations. (*a*) Results for $B_T$ [CCW] and $IB_v$ [CCW] (case 1) (*b*) Results for $B_T$ [CW] and $IB_v$ [CCW] (case 2). (*c*) Results for $B_T$ [CW]. $IB_v$ [CW] $B_T$ (case 3). The colored lines denote $I_p$ at different time points.

The variations in $I_p$ across different magnetic configurations indicate that plasma start-up can be optimized by increasing the equilibrium area ratio.

## 4. Reconstruction of the current density profile using an improved fitting model

A top–bottom symmetric current density profile model was employed to reconstruct the current density profile based on the measured magnetic flux data first. The current mainly represents a pressure driven current, $I_{pressure}$. The center of the current density located at the mid-plane and it bounded by the vacuum waveguides and plasma-facing walls. The results are shown in figure 9. The measured data was obtained in the conditions under $B_T$ [CCW] and $B_T$ [CW] configurations (case 1 and 2) with similar area ratios ($B_R$ =0 A). A wide current density profile is required for $B_T$ [CCW] (case 1), but not for $B_T$ [CW] (case 2). Significant discrepancies in peak positions between measured and modeled values are observed in both the HFS (ch1–24) and LFS (ch30–58) regions, indicating clear shifts in the magnetic flux distribution. The measured values in ch1-10 of the $B_T$ CCW configuration (case 1) show a decrease compared to the modeled values. The discrepancies indicate a shift of current density position from the mid-plane and it may represent a shift of $I_{pressure}$ and a presence of $I_{EBW}$ s with differing magnitudes and opposite directions in the upper and lower halves of the plasma.

To investigate the model sensitivity, we used both the filament current model and the strip-like current model for the expression of the EBW current distribution [22]. As a result, the difference of the model was mainly evident in the flux loop signals located on central stack, because the EBW drive current is expected to appear on the EBW absorption region where is close to the central stack. The strip has a vertically elongated rectangular shape to simulate the EBW absorption region. The filament current model suffers from problems such as excessive current concentration leading to unrealistically large distortion on the magnetic surface, and the presence of currents in the anti-equilibrium direction. This situation can also happen in the strip-like current model, because the algorithm may continuously increase the concentration of current in pursuit of minimal fitting error. Actually, the presence of anti-equilibrium current has been observed in the MAST device [19], but to avoid unrealistic distortions of the magnetic surface, this paper employs a vertically elongated elliptic current model with a current density distribution that decays from the center to the edge. Since the solution obtained from the magnetic flux loop signal is not unique, it is desirable to directly measure the current density, but that is beyond the scope of this paper.

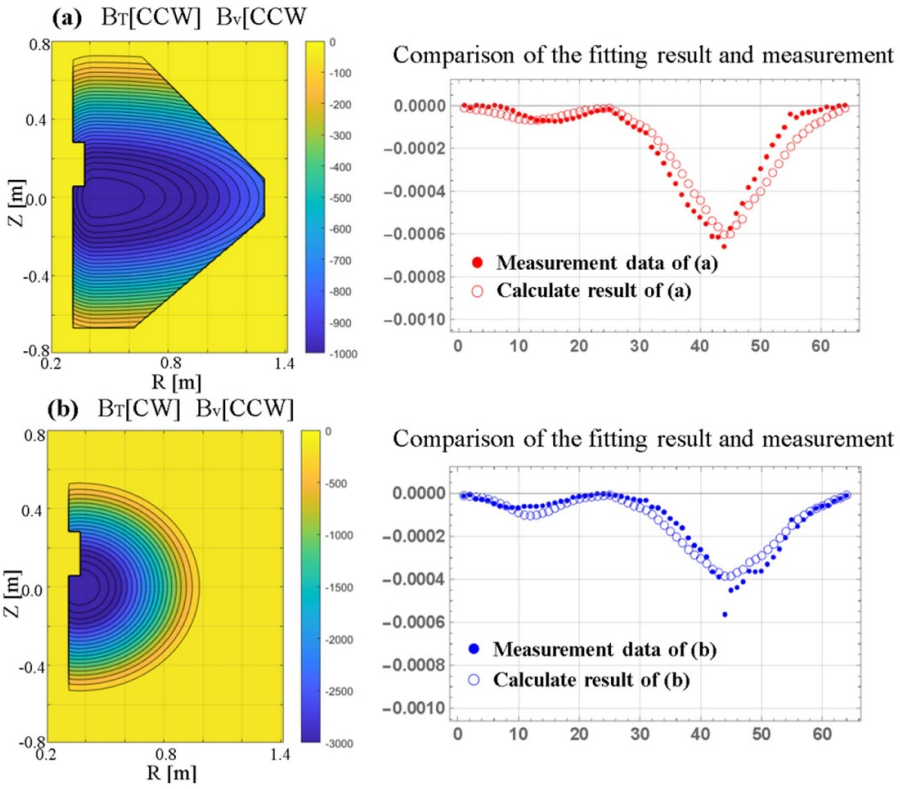


**Figure 9.** Fitting results using a top–bottom symmetric current density profile model. (*a*) Current density profile in $B_T$ [CCW] configuration (case 1) and the comparison of the fitting result and measurement. Red dots represent the measurement data and red circles represent the calculated data. (*b*) Current density profile in [CW] configuration (case 2) and the comparison of the fitting result and measurement. Blue dots represent the measurement data and blue circles represent the calculated data.

Figures 10(*a*)–(*c*) illustrate the plasma current density profile was fitted by the vertically elongated elliptic current model with the data from Ch.1–24 located on the central stack (figure 1) assigned 10 times higher weighting than those from the other channels, because these 24 signals are mainly representing the EBWCD effect. It is important to note that the direction of the EBW drive current is reversed due to the $B_T$ inversion, so the directions of the upper and lower elliptical currents are reversed. Figure 10(*e*) illustrates all measured flux signals and calculated data for both discharges. The fitting results are better than those shown in figure 9. The current density distribution shown in figure 9 also shifted upward or downward by 0.1 m in $B_T$ [CCW] and $B_T$ [CW] configurations respectively, to be fitted with flux loop signals located on the LFS. The positions of the top–bottom elliptic current density suggest the presence of the local EBW drive current. The fitting results closely match the flux loop signals, demonstrating that the direction of the EBW drive current was inverted when the is reversed. This clearly indicates that $I_{EBW}$ is present in the OFC during the start-up phase. The presence of a positive and negative pair current indicates that comparing these current distributions is necessary for accurately estimating the efficiency of EBWCD. Actually, the $I_{EBW}$ estimated by the model is 0.563 kA and the EBWCD efficiency is 0.014 A $W^{-1}$ although the net $I_{EBW}$ is 79.4 A according the following formula,

$$\eta_{\mathrm{EBWCD}} = \frac{I_{\mathrm{EBW}}^{\mathrm{total}}}{P_{\mathrm{inj}}^{\mathrm{net}}}.$$

Here the $I_{\mathrm{EBW}}^{\mathrm{total}}$ and $P_{\mathrm{inj}}^{\mathrm{net}}$ refer to the magnitude of generated EBW current in both equilibrium or anti-equilibrium direction and the difference between the injected power and reflected power of Klystrons power according the following formulas,

$$\boldsymbol{I}_{\mathrm{EBW}}^{\mathrm{total}} = \boldsymbol{I}_{\mathrm{EBW}}^{\mathrm{equ}} + \boldsymbol{I}_{\mathrm{EBW}}^{\mathrm{anti-equ}}$$
$$P_{\mathrm{inj}}^{\mathrm{net}} = P_{\mathrm{inj}} - P_{\mathrm{ref}}.$$

The efficiency of EBWCD could be further improved if the injected wave were more tightly focused, thereby minimizing the anti-equilibrium current. The applied model is useful to distinguish $I_{EBW}$ from $I_{pressure}$, but the total current should be represented by more complicated current profiles, because the $I_{EBW}$ may spread along the flux surface. In addition, total current density distribution shows an anti-equilibrium direction current locally being surrounded by an equilibrium current. The EBWCD effect is reflected in the distributed current profile within the model. From this perspective, the model effectively represents the combined contributions of the $I_{pressure}$ and the $I_{EBW}$ in the OFS phase [22], compared to the conventional models [24]. The EBW may drive both equilibrium and anti-equilibrium currents depending on the magnetic

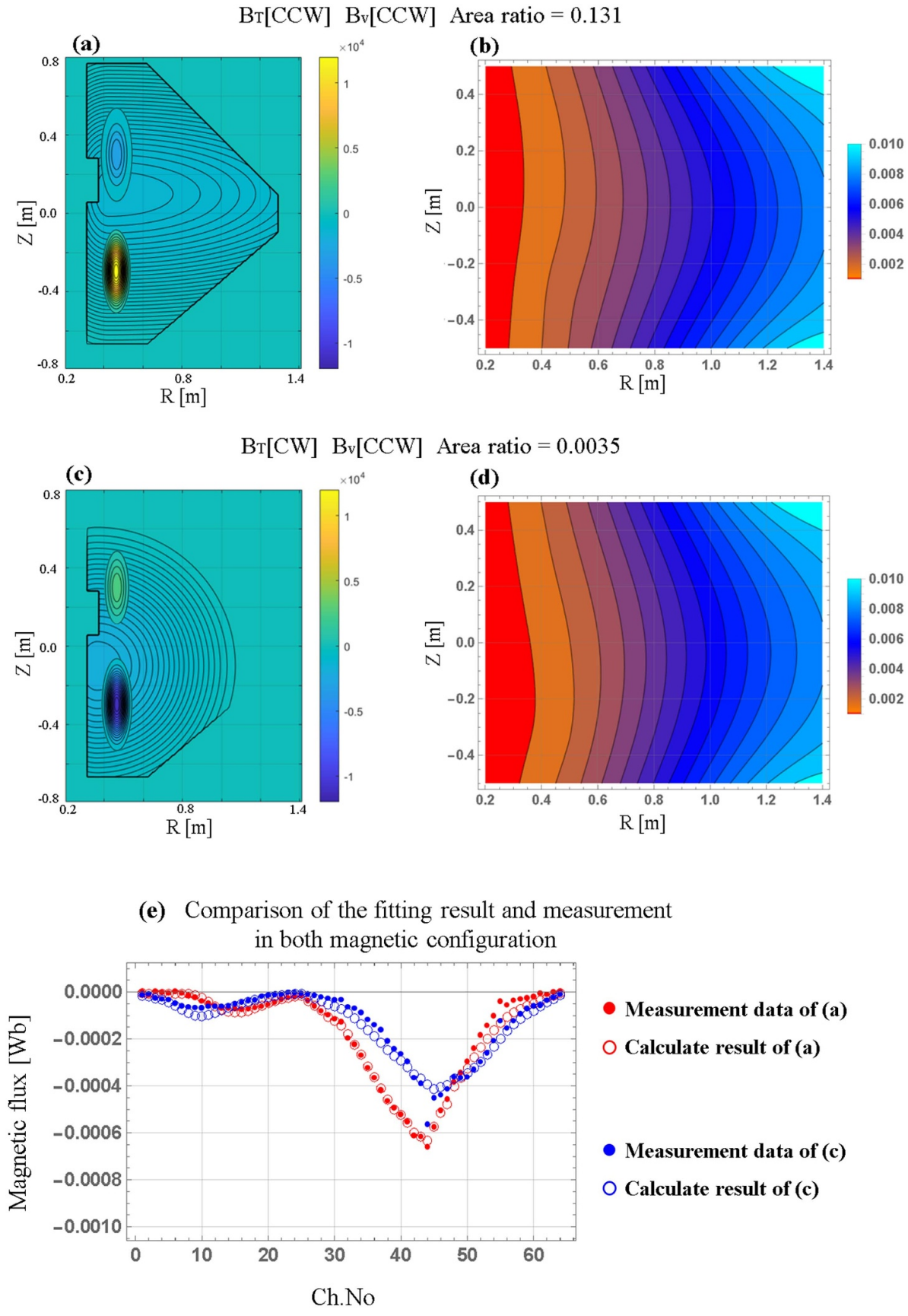


**Figure 10.** Representative fitting results using a previously described model [22]. (*a*) Shows the fitted current density distribution, with two elliptical current profiles where EBWCD is expected. (*b*) Shows the corresponding flux surfaces based on the fitted current distribution. (*c*) and (*d*) Are panels for the $B_T$ [CW] configuration; the panel descriptions are the same as in (*a*) and (*b*). (*e*) Comparison between fitting results and experimental data for both magnetic configurations.

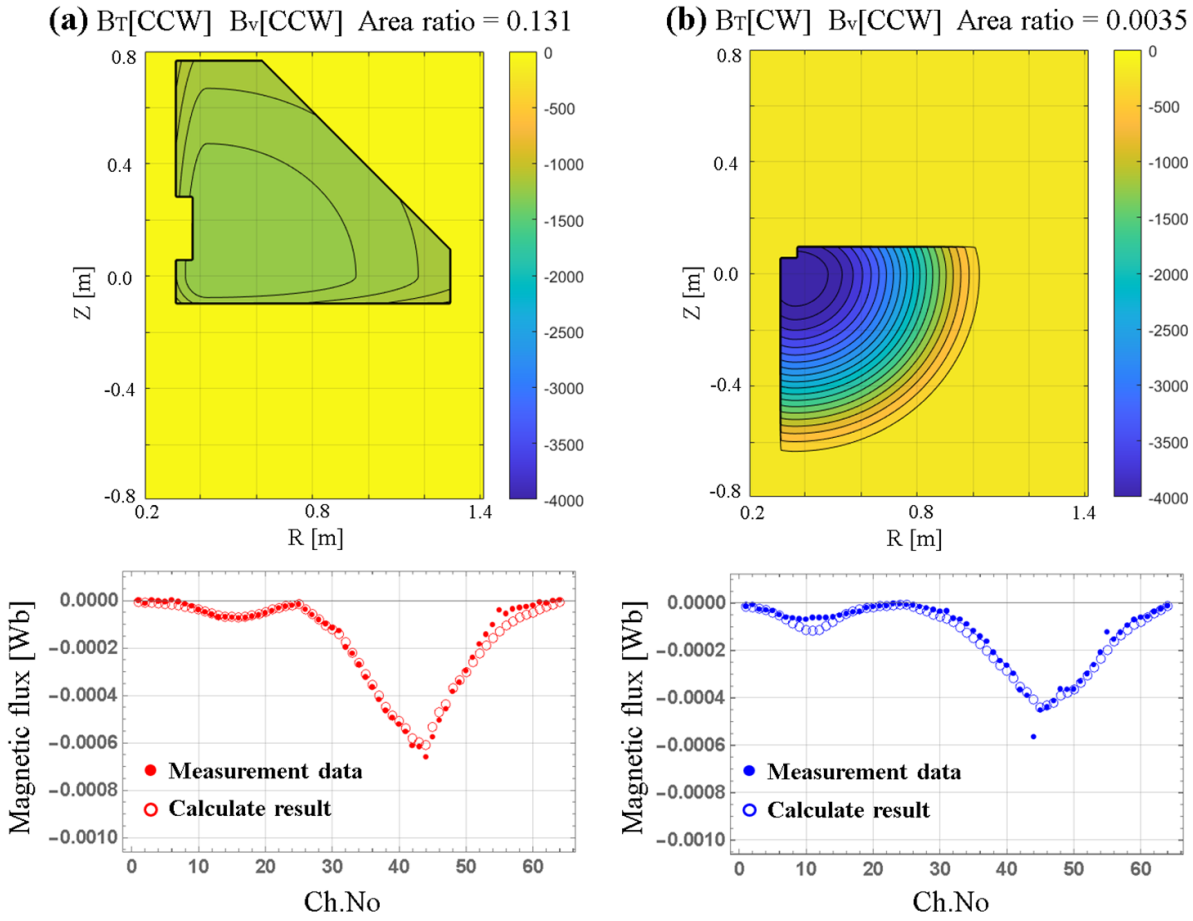


**Figure 11.** (*a*) Shows the fitted current density distribution with the current distribution model proposed by Yoshinaga, in which the current density concentrates on the upper side. (*b*) Shows the fitted current density distribution, in which the current density concentrates on the lower side.

configuration. In the anti-equilibrium area, the $I_{EBW}$ counteracted the $I_{pressure}$, although a stronger anti-equilibrium current could not be driven due to the difficulty of achieving force balance. Consequently, the distributed current in the anti-equilibrium area was weakened by the generated EBW current.

Considering that the anti-equilibrium $I_{EBW}$ in figures 10(*a*)–(*c*) may partially cancel with the $I_{pressure}$, figures 11(*a*) and (*b*) presents the fitting results using the current distribution model proposed by Yoshinaga *et al* [24] that prohibits the presence of anti-equilibrium current as a total value. In the $B_T$ [CCW] (case 1) and $B_T$ [CW] (case 2) configurations, the current concentrates in the upper and lower halves of the vessel, respectively, with no current present in the opposite side. This indicates that the anti-equilibrium $I_{EBW}$ causes a significant decrease in current density as a total value. As a result, the fitting results exhibit a half-sided current profile. In addition, the calculated flux in $B_T$ [CW] (case 2) shows a large difference around Ch.10, where is close to the mid-plane. A more complicated current distribution model may be necessary to reconstruct accurate current density profile. Only the flux loop signals are insufficient, and further research will require obtaining two-dimensional information including the inside of the plasma, which is beyond the scope of this paper.

Figure 12 shows the currents contained in the equilibrium and anti-equilibrium areas plotted as a function of the area ratio induced by the variation of $B_R$ at 0.02 s after RF injection. In this analysis, the current distribution model proposed in the [22] is used to more easily search for trends. The currents in the equilibrium area exhibited the same trend with respect to the area ratio variation—-namely, the larger the ratio, the greater the current. In contrast, the currents in the anti-equilibrium area remained nearly constant with a slightly positive value as the area ratio increased under the $B_T$ [CCW] configuration (case1). In the $B_T$ [CW] configuration (case 2), the sign of the current in the anti-equilibrium area reversed around the area ratio of approximately zero. This finding is particularly significant, as EBWCD cannot drive equilibrium current in the anti-equilibrium area. Although the area ratio is defined based on the vacuum magnetic field, it is expected to shift toward more negative values when considering magnetic field variation induced by the driven current. This suggests the presence of other driven current components, such as ECCD and currents driven by energetic electrons in the OFC. The effect of energetic electron was negligible, because the electron density, $n_e$ was 5 times larger than that in the discharge where energetic electrons dominantly drive $I_p$ [25]. The injected ECW from the antenna expanded toroidally and poloidally, and the

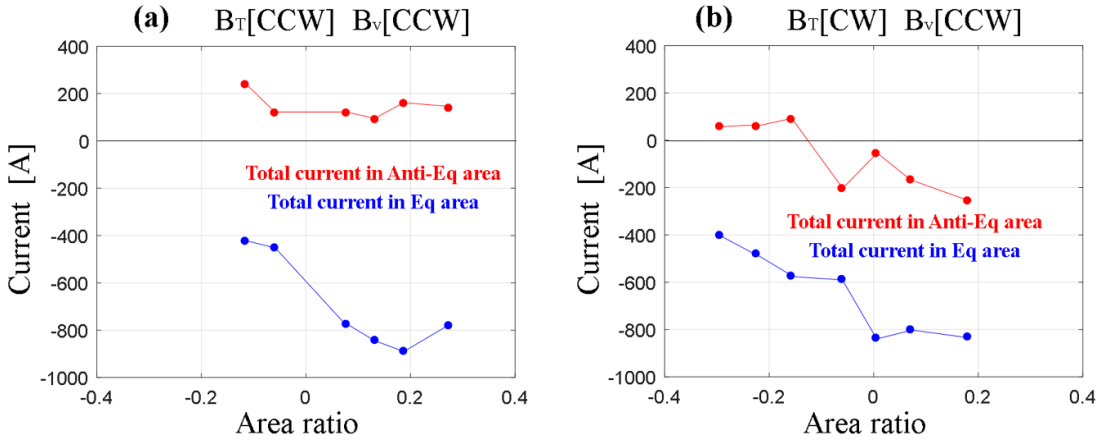


**Figure 12.** Current flowing at 0.02 s in the equilibrium area based on the vacuum field (red circles and lines) and in the anti-equilibrium area (blue circles and lines) as a function of area ratio induced by a variation of $B_R$, according to the fitting result derived from the current distribution model [22].

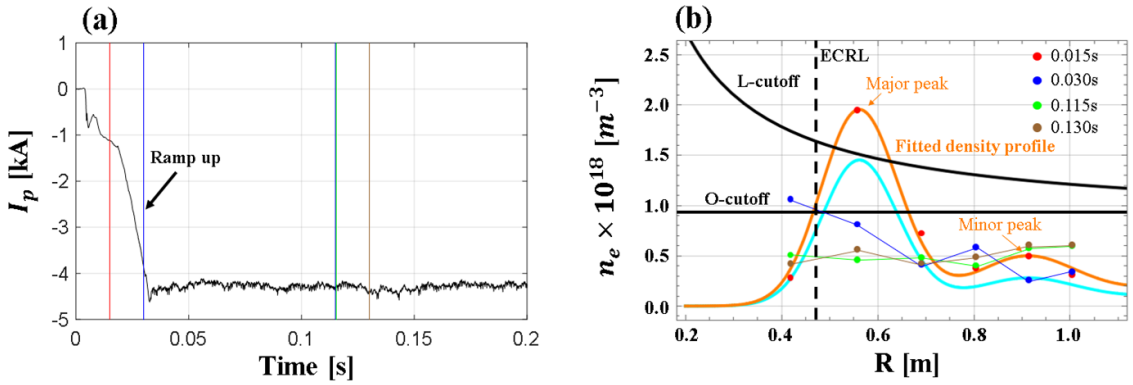


**Figure 13.** (*a*) Time evolution of plasma current. (*b*) $n_e$ profiles measured with Thomson scattering at the time points indicated through the colored lines in panel (*a*). Two black lines of plasma cutoff ($(\omega_{pe}/\omega)^2 \cong 1$) and L cutoff for $N_{tor} = 0$, are indicated in panel (*b*). The orange curve represents the fitting result of the Thomson scattering measurement obtained using a two-peak Gaussian model, and corresponding to the point 2(Orange symbols) in figure 4(*b*). The major and minor peaks are indicated with orange arrows. The cyan curve represents the density profile when the L cut-off layer just disappears, corresponding to the point 3 (Cyan symbol) in figure 14(*b*). $\omega_{pe}$, electron plasma frequency; $\omega$, wave frequency; $N_{tor}$, refractive index in the toroidal direction.

ECW may be absorbed at the 1st ECR layer as X-mode, but the absorption of X-mode in the vicinity of plasma cut-off density is small [26]. The ECCD effect may cancel out in toroidal directions, but the equilibrium current is likely to remain more effective in the OFC [21]. Otherwise, a small closed magnetic flux surface may have formed at the time, because the total $I_p$ was larger than the others. This may be related to the $I_p$ ramp-up (figure 6).

## 5. Inference of ECW propagation based on reconstructed current density profile

To clarify the difference in the current ramp-up between the two directions of the $B_T$ as shown in figure 6, the time evolution of $n_e$ and the consequent change of the UHR layer were analyzed. The $n_e$ profile was reconstructed based on Thomson scattering measurements. The $n_e$ was assumed to be constant along each magnetic flux surface. According to the radial $n_e$ profile measured with a movable Langmuir probe inserted into the plasma [26], a major peak and a sub-peak were observed. The major peak, located a little low field side of the 1st ECR of the injected ECW, exhibited a significantly higher $n_e$ during the OFS phase (figure 13(*b*)). The sub-peak, located around $R$ =0.915 m, was noticeably higher than that of the surrounding regions.

As the time evolution of $n_e$ could not be measured due to the insufficient temporal resolution of the Thomson scattering diagnostic, an interferometer signal was used to estimate the time evolution of the line-averaged $\bar{n}_e$ along the mid-plane in the OFS (figure 14).

Corresponding to the distinct time evolution of the current ramp-up in the OFS, the $\bar{n}_e$ also exhibited different temporal behavior. The $\bar{n}_e$ sharply increased immediately after the ECW injection and then decreased to approximately $5 \times 10^{17}$ m$^{-3}$. When the current increased continuously, the $\bar{n}_e$ remained constant after reaching $5 \times 10^{17}$ m$^{-3}$ (figure 14(*a*)). This time evolution of $I_p$ is typically observed in the case of $B_T$[CW], where the equilibrium current driven by EBW was expected to form on the lower side. Figure 14(*b*) shows

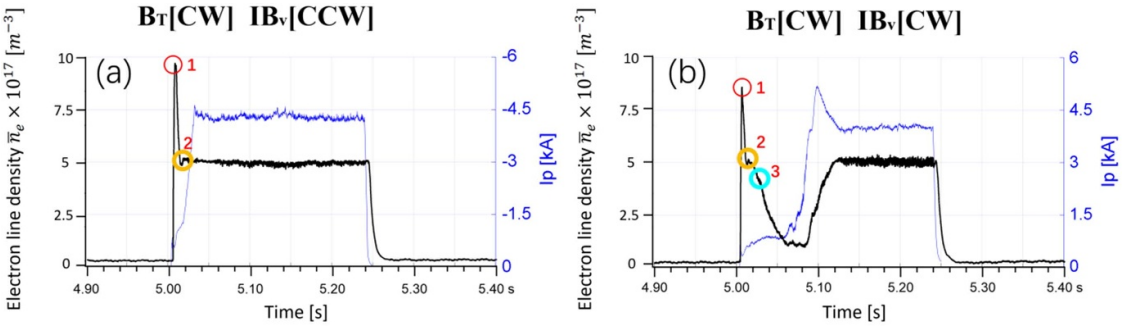


**Figure 14.** Typical time evolutions of $I_p$ (black line) and $\overline{n_e}$ (blue line) regarding (*a*) smoothed current ramp-up under $B_T$ [CW], $B_V$ [CCW], $IB_R = -20$ A, and (*b*) current jump under $B_T$ [CW], $B_v$ [CW], $IB_R = -20$ A are denoted. In both cases, reached high $n_e$ just after ECW injection. The red, orange and cyan symbols indicate the time points corresponding to the 2D map (figure 15).

the representative time evolutions of $I_p$ and $\bar{n}_e$. The flat-top values of $I_p$ and $\bar{n}_e$ were similar in both cases. This finding suggests that the flat-top values of $I_p$ and $\bar{n}_e$ were primarily maintained by other CD mechanisms rather than by EBWCD. If the EBWCD had been the dominant CD mechanism, the equilibrium current would likely have flowed in front of the antenna, which was positioned on the upper side. Identifying which CD mechanism predominantly operated after the formation of the CFS remains a subject for future investigation.

When the current did not ramp up and remained almost constant before the current jump (figure 14(*b*)), the $\bar{n}_e$ continuously decreased to approximately $1.2 \times 10^{17}$ m$^{-3}$ and then increased concurrently with the rise in $I_p$.

At the beginning of the RF injection, since the high plasma density $[(\omega_{pe}/\omega)^2 > 2]$, an L-cutoff layer formed in front of the antenna, causing all the X-mode ECW to be reflected back (figure 15(*a*)). Consequently, $n_e$ decreased, and the L-cutoff layer contracted accordingly. As $n_e$ continued to decrease, the L-cutoff layer further reduced in size (figure 15(*b*). However, calculation of the L-cutoff and UHR layers was based solely on $n_e$ measured on the mid-plane with Thomson scattering. The 2D density profile over the poloidal cross-section was not available. The calculation of the L-cutoff layer was conducted under the assumption that $n_e$ is constant on the flux surface. Since the value of $n_e$ in front of the antenna may be larger than that on the mid- plane, the L-cutoff layer is more likely to form in front of the antenna.

The L-cutoff layer gradually contracted and moved outward as $\bar{n}_e$ decreased. When $\bar{n}_e$ reached $5 \times 10^{17}$ m$^{-3}$, the L-cutoff layer was reduced, allowing the ECW emitted from the antenna to be reflected upon reaching the L-cutoff layer and then reflected again via the central stack, ultimately reaching the equilibrium area below the mid-plane. Consequently, the $\bar{n}_e$ might be keeping a distinct plateau at $5 \times 10^{17}$ m$^{-3}$ in the balance of in the balance of ECW propagation and EBW absorption as shown in figures 14(*a*) and (*b*) (symbol 2).

After $\bar{n}_e$ reached $5 \times 10^{17}$ m$^{-3}$, the L-cutoff layer disappeared or remained, leading to different plasma responses. When the L-cutoff layer was maintained at $\bar{n}_e = 5 \times 10^{17}$ m$^{-3}$, the EBW was continuously absorbed in the equilibrium area and coupled with $I_{pressure}$, resulting in the ramp-up of $I_p$. It should be noted that the elimination of L-cutoff takes place in lower $n_e$ for higher $N//$.

$$1 - \frac{\omega_p^2}{\omega\left(\omega - \omega_{ce}\right)} - N_{\|}^2 = 0$$

$$\omega_p^2 = \frac{n_e e^2}{\varepsilon_0 m_e}.$$

If the L-cutoff layer disappeared (figure 15(*c*)), the EBW would be absorbed in the anti-equilibrium area located above the mid-plane in the case of $B_T$[CW] (case 2). The resulting $I_{EBW}$, flowing opposite to $I_{pressure}$, inhibited the formation of CFS. Consequently, $I_p$ remained constant, while $\bar{n}_e$ continued to decrease, as indicated at the time marked as symbol 3 in figure 14(*b*). As decreased further, L-cutoff for ECW with higher $N_{//}$ gradually eliminated and the UHR layer moved inward, and the closer the UHR layer approached the antenna, the more concentrated the EBW absorption became.

Figure 16 depicts the comparison results of $I_p$ at 0.03 s. Regarding $B_T$ [CCW] $B_v$ [CCW] (case 1), the injected ECW was reflected toward the lower side, corresponding to the anti-equilibrium area, by the presence of L-cutoff layer. This reflected ECW hindered the formation of CFS, and the $I_p$ remained constant and subsequently jumped to its maximum once $I_p$ became sufficient to form the CFS.

Regarding [CW] (case 2), following the initial density surge, the L-cutoff layer gradually contracted as the density decreased. The injected ECW was reflected into the equilibrium area below the mid-plane, where it was converted into EBW and subsequently absorbed, generating an equilibrium current that contributes to $I_p$. Consequently, the $I_p$ growth rate significantly exceeded that observed in the $B_T$ [CCW] case as shown in figure 6(*a*).

The plasma start-up under a negative area ratio was unstable. Regarding $B_T$ [CW], plasma failed to start up (figures 8(*b*) and (*c*)), but later succeeded (figure 14(*b*)). The reason is attributed to the time evolution of $n_e$ as described above. The fuel hydrogen absorbed in the first wall after several days of experiments may have an impact, but the true reason remains unknown. Since the area ratio was negative (red arrow), the plasma start-up was not achieved until 0.1 s after injection,

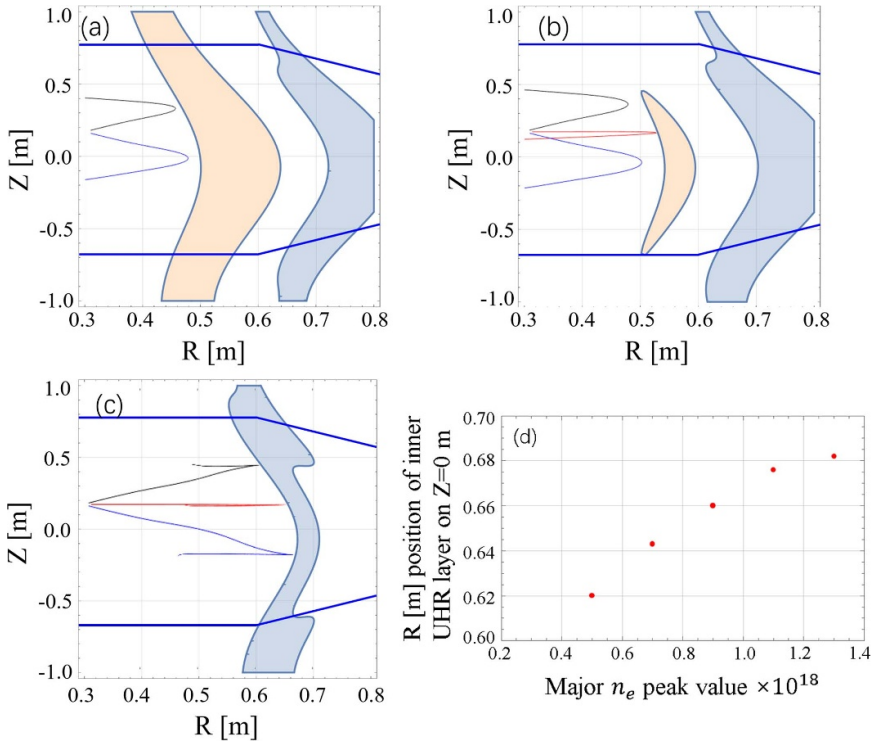


**Figure 15.** The thick blue lines represent the waveguides inside the vacuum vessel. The light orange area represents the L-cutoff layer for $N_{//}$ =0. The light blue area represents the non-propagating area for ECW X-mode between the UHR layer on the high-field side and the *R* cutoff layer on the low-field side. The thin black lines, red lines and blue lines represent the path of the injected waves according to $\frac{k_Z}{k_R} = 1$, $\frac{k_Z}{k_R} = 0$ and $\frac{k_Z}{k_R} = -1$, respectively, under different electron density profiles. (*a*) $\bar{n}_e = 8.6 \times 10^{17}$ m$^{-3}$, corresponding to symbol 1 in figure 14. (*b*) $\bar{n}_e = 6 \times 10^{17}$ m$^{-3}$, corresponding to symbol 2 in figure 14(*c*) $\bar{n}_e = 4.2 \times 10^{17}$ m$^{-3}$, corresponding to symbol 3 in figure 14. (*d*) The *R* position of the UHR layer on $Z = 0$ m, corresponding to the major $n_e$ peak value. **Abbreviations:** L-cutoff, left-hand-cutoff; UHR, upper hybrid resonance; *R*-cutoff, right-hand-cutoff; *R*, radial

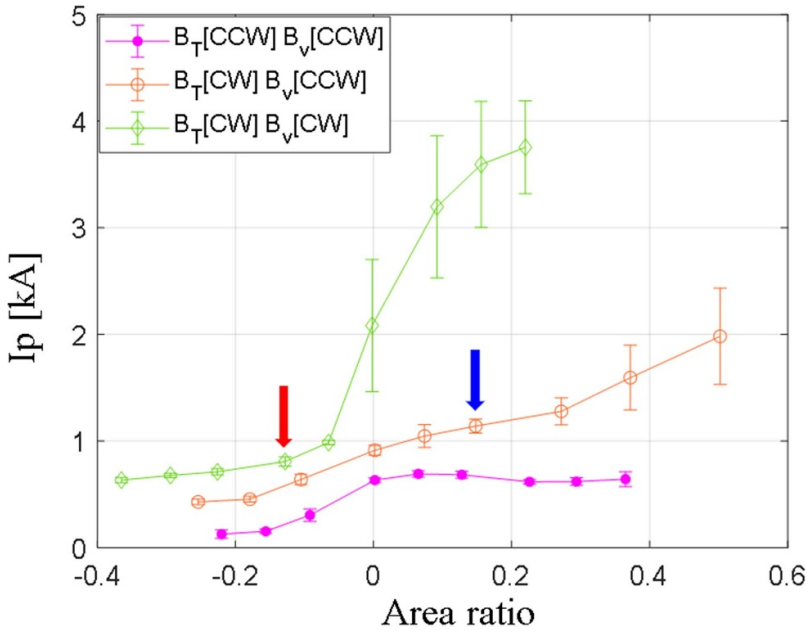


**Figure 16.** Comparison of $I_p$ at 0.03 s under different magnetic configurations shown in figure 8. The pink (case 3), orange (case 2) and green (case 1) marks represent the total plasma current in different magnetic field configuration, respectively. The blue arrow indicates the equilibrium area ratio corresponding to figure 11(*a*), while the red arrow indicates the equilibrium area ratio corresponding to figure 14(*b*).

which was considerably slower than that observed in the positive area ratio (blue arrow). This finding indicates that the equilibrium area ratio exerts a significant influence on plasma start-up behavior.

## 6. Summary

EBWCD experiments using the HFS injection system were conducted on the QUEST device. During the experiments, $B_T$ was reversed from CCW to CW. Consequently, the peak of the measured magnetic flux at the central stack shifted from the top side to the bottom side, indicating that a part of the equilibrium $I_p$ was driven via EBW. The appearance of opposite magnetic flux on the anti-equilibrium side further confirmed the presence of anti-equilibrium EBWCD.

The $B_v$ and $B_R$ were also adjusted to further investigate plasma start-up. The shift of the plasma mid-plane caused by varying $B_R$ affected the balance between the equilibrium and anti-equilibrium areas of the $I_{EBW}$ relative to the $I_{pressure}$. The results show that when the anti-equilibrium area was larger than the equilibrium area, plasma start-up became significantly more difficult or failed altogether. In the $B_T$ [CW] configuration, the CFS formed earlier owing to the larger equilibrium area ratio. The $I_p$ always grew faster and more smoothly than in the $B_T$ [CCW] configuration during the OFS phase. This may be because the L-cutoff layer appeared before the antenna located on the top side, preventing the propagation of the ECW and thereby reducing the EBWCD contribution to $I_p$.

The current density profile was then reconstructed using an improved model based on the measured magnetic flux distribution. On the ant-equilibrium side, the EBWCD and $I_{pressure}$ may have partially canceled each other, while the equilibrium EBWCD concentrated the $I_p$ on the upper or lower side depending on the $B_T$ configuration. The total EBWCD was estimated via assuming the same $I_{pressure}$ under similar magnetic configuration, yielding an efficiency of approximately 0.014 A $W^{-1}$ in the OFS phase. However, this calculated EBWCD efficiency does not represent the pure current-drive efficiency for $I_p$ start-up, but rather indicates the magnitude of the $I_{EBW}$.

By evaluating the currents on both sides of the plasma mid-plane, it was observed that the current in the anti-equilibrium area exhibited different behavior under the $B_T$ [CCW] and $B_T$ [CW] configurations. The reason may be attributed to the existence of the L-cutoff layer during the early phase of plasma start-up, which would have prevented the propagation of the ECW and reflected it toward the bottom side of the vacuum vessel. In the $B_T$ [CCW] configuration, the current in the anti-equilibrium area did not vary significantly with changes in the equilibrium area ratio. In the [CW] configuration, when the equilibrium area ratio increases, the current in the anti-equilibrium area decreased significantly and transitioned from positive to negative values. This indicates that within the anti-equilibrium area, the value of $I_{pressure}$ has surpassed the anti-equilibrium $I_{EBW}$. This phenomenon may be attributed to the antenna's position above the equatorial plane.

The L-cutoff and UHR layers were also reconstructed based on the measured $n_e$. The calculated variation of the L-cutoff layer, corresponding to changes in the line-averaged $\overline{n_e}$, indicating that the L-cutoff layer appeared at the beginning of plasma start-up and prevented the propagation of all ECW. The L-cutoff layer gradually contracted as $n_e$ decreased and eventually disappeared just before reaching the antenna position. Subsequently, the $\overline{n_e}$ decreased continuously, corresponding to the smooth ramp-up of $I_{p,}$ or remained constant, corresponding to the sudden jump of $I_p$. This may be attributed to the different initial $n_e$ profiles, as the major and minor peaks significantly influence the location and shape of the UHR layer, leading to distinct subsequent variations in $n_e$ and $I_p$. However, the calculation results deviate from the experimental values because only the $n_e$ distribution on the equatorial plane was measured.

In conclusion, EBWCD via HFS injection played an important role in plasma start-up; however, the anti-equilibrium current reduced the net efficiency of EBWCD. The anti-equilibrium current could cancel a part of widespread $I_{pressure}$ and resulted in current density concentration which played a role in a CFS formation. Minimizing the anti-equilibrium current remains an important challenge and a promising approach for future ST-based fusion reactors.

## Acknowledgments

The authors are most thankful to the QUEST team for their technical support. We thank M Fukuyama from Kyushu University for providing measurement data by interferometer, and Y Peng from the University of Tokyo for providing measurement data by Thomson scattering. We thank Y Wang from Kyushu University for his valuable comments. This work was supported by a Grant-in-Aid for the Japan Society for the Promotion of Science (JSPS) Fellows (KAKENHI Grant Number 21H04456) and the NIFS Collaboration Research Program (NIFS19KUTR136).

## ORCID iDs

Hanada Kazuaki 0000-0001-5045-9782
Onchi Takumi 0000-0001-8821-0296
Kojima Shinichiro 0000-0001-6933-5579
Yue Qilin 0009-0006-1917-0132
Kuroda Kengoh 0000-0003-2451-4893
Ido Takeshi 0000-0003-1098-2565
Ikezoe Ryuya 0000-0003-2615-1256
Idei Hiroshib 0000-0001-6282-4521
Nagashima Yoshihiko 0009-0002-5513-9723
Kinoshita Toshiki 0000-0003-3930-4434

## References

[1] Peng Y.K.M. 2000 *Phys. Plasmas* **7** 1681–92
[2] Takase Y. *et al* 2011 *Nucl. Fusion* **51** 063017
[3] Luce T.C., Lin-Liu Y.R., Harvey R.W., Giruzzi G., Politzer P.A., Rice B.W., Lohr J.M., Petty C.C. and Prater R. 1999 *Phys. Rev. Lett.* **83** 4550

[4] Bernstein I.B. 1958 *Phys. Rev.* **109** 10
[5] Ram A.K. and Schultz S.D. 2000 *Phys. Plasmas* **7** 4084–94
[6] Taylor G, Efthimion P.C., Kessel C.E., Harvey R.W., Smirnov A.P., Ershov N.M., Carter M.D. and Forest C.B. 2004 *Phys. Plasmas* **11** 4733–9
[7] Urban J., Decker J., Peysson Y., Preinhaelter J., Shevchenko V., Taylor G., Vahala L. and Vahala G. 2011 *Nucl. Fusion* **51** 083050
[8] Bilato R., Volpe F., Köhn A., Paccagnella R., Farina D., Poli E. and Brambilla M. 2009 *Nucl. Fusion* **49** 075020
[9] Uchida M., Noguchi Y., Tanaka H. and Maekawa T. 2015 *EPJ Web Conf.* vol 87 p 02006
[10] Laqua H.P., Erckmann V., Hartfuß H.J. and Laqua H 1997 *Phys. Rev. Lett.* **78** 3467
[11] Shiraiwa S. *et al* 2006 *Phys. Rev. Lett.* **96** 185003
[12] Jo J. *et al* 2017 *Phys. Plasmas* **24** 1–9
[13] Yoneda R., Hanada K., Eiserafy H., Bertelli N. and Ono M. 2018 *Plasma Fusion Res.* **13** 3402115
[14] Elserafy H. *et al* 2019 *Plasma Fusion Res.* **14** 1205038
[15] Kojima S. 2021 Advanced plasma current start-up using RF heating for Tokamak fusion plasma (Kyushu University)
[16] Shevchenko V., Baranov Y., O'Brien M. and Saveliev A. 2002 *Phys. Rev. Lett.* **89** 265005
[17] Shevchenko V., Cunningham G., Gurchenko A., Gusakov E., Lloyd B., O'Brien M., Saveliev A., Surkov A., Volpe F. and Walsh M. 2007 *Fusion Sci. Technol.* **52** 202–15
[18] Shevchenko V.F. *et al* 2015 *EPJ Web of Conf.* vol 87 p 02007
[19] Shevchenko V.F., O'Brien M.R., Taylor D. and Saveliev A.N. and (MAST Team) 2010 *Nucl. Fusion* **50** 022004
[20] Tanaka H. *et al* 2018 Noninductive production of extremely overdense spherical tokamak plasma by electron Bernstein wave excited via O-X-B method in LATE *IAEA Fusion Energy Conf. (FEC 2016)* (*Kyoto*) p 289
[21] Maekawa T., Tanaka H. and Uchida M. 2019 *Plasma Phys. Control. Fusion* **61** 105017
[22] Junyao Z., Hanada K., Kuroda K., Onchi T., Idei H., Ikezoe R., Hasegawa M., Nagashima Y., Ido T. and Kinoshita T. 2024 *Evergreen* **11** 555–62
[23] Yoshinaga T., Uchida M., Tanaka H. and Maekawa T. 2006 *Phys. Rev. Lett.* **96** 125005
[24] Yoshinaga T., Uchida M., Tanaka H. and Maekawa T. 2007 *Nucl. Fusion* **47** 210
[25] Ishiguro M. *et al* 2012 *Phys. Plasmas* **19** 6
[26] Murakami T. *et al* 2024 *Plasma Phys. Control. Fusion* **66** 115016